Deposition of hydrophilic $Ti_3C_2T_x$ on a superhydrophobic ZnO nanorod array for improved surface-enhanced raman scattering performance

Zhihua Wu[1], De Zhao[1], Xin Han[3], Jichang Liu[3], Ying Sun[1*], Yaogang Li[2*] and Yourong Duan[1*]

Abstract

Background Superhydrophobic substrate modifications are an effective way to improve SERS sensitivity by concentrating analyte molecules into a small surface area. However, it is difficult to manipulate low-volume liquid droplets on superhydrophobic substrates.

Results To overcome this limitation, we deposited a hydrophilic $Ti_3C_2T_x$ film on a superhydrophobic ZnO nanorod array to create a SERS substrate with improved analyte affinity. Combined with its interfacial charge transfer properties, this enabled a rhodamine 6G detection limit of 10^{-11} M to be achieved. In addition, the new SERS substrate showed potential for detection of biological macromolecules, such as microRNA.

Conclusion Combined with its facile preparation, the SERS activity of $ZnO/Ti_3C_2T_x$ suggests it may provide an ultra-sensitive environmental pollutant-monitoring and effective substrate for biological analyte detection.

Keywords SERS, Superhydrophobic substrate, $Ti_3C_2T_x$, DFT calculations, miRNA detection

*Correspondence:
Ying Sun
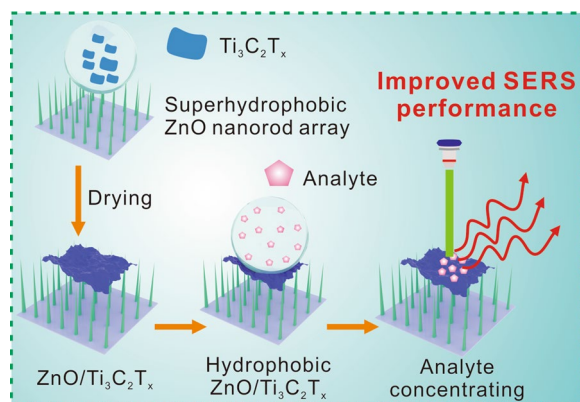ysun@shsci.org
Yaogang Li
yaogang_li@dhu.edu.cn
Yourong Duan
yrduan@shsci.org
Full list of author information is available at the end of the article

Wu *et al. Journal of Nanobiotechnology*   (2023) 21:17

Page 2 of 11

Graphical Abstract

Introduction

Surface-enhanced Raman scattering (SERS) is a widely used and powerful tool for analyzing molecules and biomarkers [1], in vivo imaging [2], and environmental pollutants [3–6]. Recent development of new surface-enhancing materials and methods has markedly improved SERS detection limits [7–9]. Notably, the combination of nanostructured plasmics and Raman spectroscopy has enabled single molecule detection [10–12]. However, the surface enhancement is restricted to "hot spots" with an area of a few nm^2 [13–16]. The detection or identification of low-concentration analytes remains challenging because random diffusion of molecules on the hydrophilic substrate results in poor spatial localization [17]. This random diffusion makes it time-consuming to search for molecules of interest within the enhanced area [18, 19].

Various strategies have been used to overcome the above problems [20–22], such as the use of superhydrophobic substrates to markedly enhance SERS intensity [17, 23–26]. Such substrates overcome the diffusion limit by concentrating molecules into a small area, resulting in a threefold increase in Raman intensity compared with ordinary hydrophilic substrates [23]. Superhydrophobic substrates can be fabricated using photolithography and those noble metal nanoparticle decorated SERS platform can achieve a detection limit of 10^{-18} M using rhodamine 6G (R6G) as a SERS probe [17]. However, the fabrication processes are sophisticated and the required equipment is expensive. Thus, more facile methods are required to prepare SERS substrates that confine the analyte molecule. Manipulating the morphology of inorganic nanoarrays may lead to new superhydrophobic substrates [27]. Among these inorganic materials, ZnO is an ideal candidate because it enables the facile synthesis and regulation of nanostructures [28]. Moreover, it can be easily decorated on the surface of different substrates, such as glass slides [29] and polydimethylsiloxane [30]. Although superhydrophobic SERS substrates can increase the Raman intensity remarkably, their poor affinity for aqueous analytes makes these molecules difficult to attach, which reduces the efficiency of the detection process.

Herein, we report a facile method to fabricate a SERS substrate comprising a two-dimensional (2D) $Ti_3C_2T_x$ monolayer on a supporting superhydrophobic ZnO nanorod array (Fig. 1). The hydrophilicity of the $Ti_3C_2T_x$ surface increases the affinity of aqueous analytes and its intrinsic metallic conductivity and plasmon resonance enhance Raman scattering intensity [31–33]. We prepared a small-area $Ti_3C_2T_x$ spot on a superhydrophobic ZnO nanorod array and demonstrated that the hydrophobic substrate concentrates the analyte within the enhancement area and thus greatly improves the Raman scattering intensity. Density functional theory (DFT) calculations further showed that the interfacial charge transfer also contributes to the intensity enhancement. The $ZnO/Ti_3C_2T_x$ substrate provides a cost-effective SERS platform for ultrasensitive analyte detection and identification.

Material and methods

Material

LiF was purchased from Aladdin Reagents (Shanghai), 200 mesh MAX Ti_3AlC_2 was purchased from 11 technology co.,LTD, hydrochloric acid (HCl), Zinc nitrate hexahydrate ($Zn(NO_3)_2$), Hexamethylenetetramine (HMTA), potassium permanganate were purchased from Sinopharm Chemical Reagent Co. Ltd. (China), Rhodamine 6G (R6G), methylene blue (MB), acid blue (AB), crystal violet (CV) were purchased from MACKLIN. All
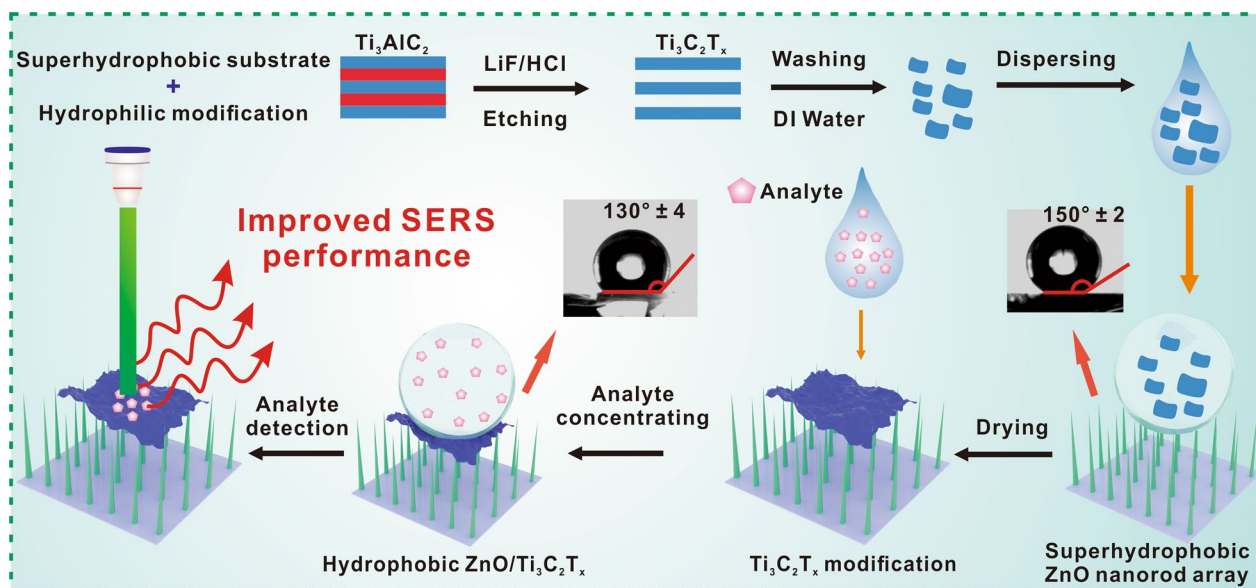
Fig. 1 Illustration of the fabrication of a $ZnO/Ti_3C_2T_x$ substrate and the mechanism of its surface-enhanced Raman scattering (SERS) activity. The $Ti_3C_2T_x$ monolayer is prepared using a selective etching method and then dispersed in deionized water. The $ZnO/Ti_3C_2T_x$ substrate is fabricated by depositing the $Ti_3C_2T_x$ solution on a superhydrophobic ZnO nanorod array

chemicals were used as received without further purification. miRNA with sequence of UUUGUACUACACAAA AGUACUG (sense(5'-3')) was purchased from RIBOBIO co.,LTD.

Fabrication of monolayer $Ti_3C_2T_x$

Monolayer $Ti_3C_2T_x$ was obtained as previously described [34, 35]. Typically, 1.6 g LiF was added in 20 mL 9 M HCl in 5 min and magnetic stirred for another 5 min. Then, 1 g Ti_3AlC_2 was added over the course of 5 min in case of overheat. Etching was performed at room temperature for 24 h. The acidic mixture was centrifugated at 3500 rpm until pH $\geq$ 5 (each cycle for 5 min). Sediment was re-dispersed by hand-shaking every time. The $Ti_3C_2T_x$ colloid was collected when the supernatant turned stable dark-green. After that, monolayer $Ti_3C_2T_x$ was collected after centrifugation at 3500 rpm for 1 h by collecting the supernatant.

Preparation of $ZnO/Ti_3C_2T_x$ SERS substrate and enhancement performance

Glass slides were pretreated using potassium permanganate and n-butanol as described previously [36]. To successfully construct ZnO nanorods on the glass slide surface, the pretreated glasses were firstly encapsulated by PDMS to form a 75 mm $\times$ 4 mm $\times$ 1 mm microchannel. Then, reaction solutions of 0.05 M $Zn(NO_3)_2$ and 0.05 M HMTA were injected by pump in two Teflon tubes at 50 μL/min for 2 h at 90 ℃ [37, 38]. After that, PDMS was removed and the obtained ZnO decorated

glass slide was thoroughly washed by distilled water. The ZnO decorated glass slide was then dried in oven at 90 ℃ for further use. ZnO film was prepaered as previously described[39].

To fabricate $ZnO/Ti_3C_2T_x$ SERS substrate, 4 μL 1–2 mg/mL monolayer $Ti_3C_2T_x$ aqueous solution was dropped onto ZnO decorated glass slide and dried at room temperature for further use. Before test, 4 μL 10^{-6} to 10^{-10} M R6G was dropped on the $ZnO/Ti_3C_2T_x$ SERS substrate and dried at room temperature. Laser of 532 nm was used in the experiments at power of 5 mW with a static mode and 20 s exposure time to reduce background noise. As for Raman mapping, step of 1 μm and 2 s exposure time at 532 nm were adopted.

DFT simulations and calculations

First-principles calculations of the enhancing mechanism in our systems used the DFT-based projector augmented-wave method implemented in the Materials Studio software [40]. The exchange–correlation energy was treated using the generalized gradient approximation of Perdew, Burke, and Ernzerhof [41, 42]. The energy cutoff for the plane wave basis expansion was set to 400 eV during the geometry relaxation. The $3 \times 3 \times 1$ Monkhorst–Pack k-point sampling grid was used to calculate the surface structures. The self-consistent calculations used an energy convergence threshold of 10^{-5} eV. The equilibrium lattice constants were optimized using a maximum stress constraint of 0.03 eV/Å on each atom. Spin polarization was allowed in all calculations. The Ti_3C_2

Wu *et al. Journal of Nanobiotechnology*   (2023) 21:17

Page 4 of 11
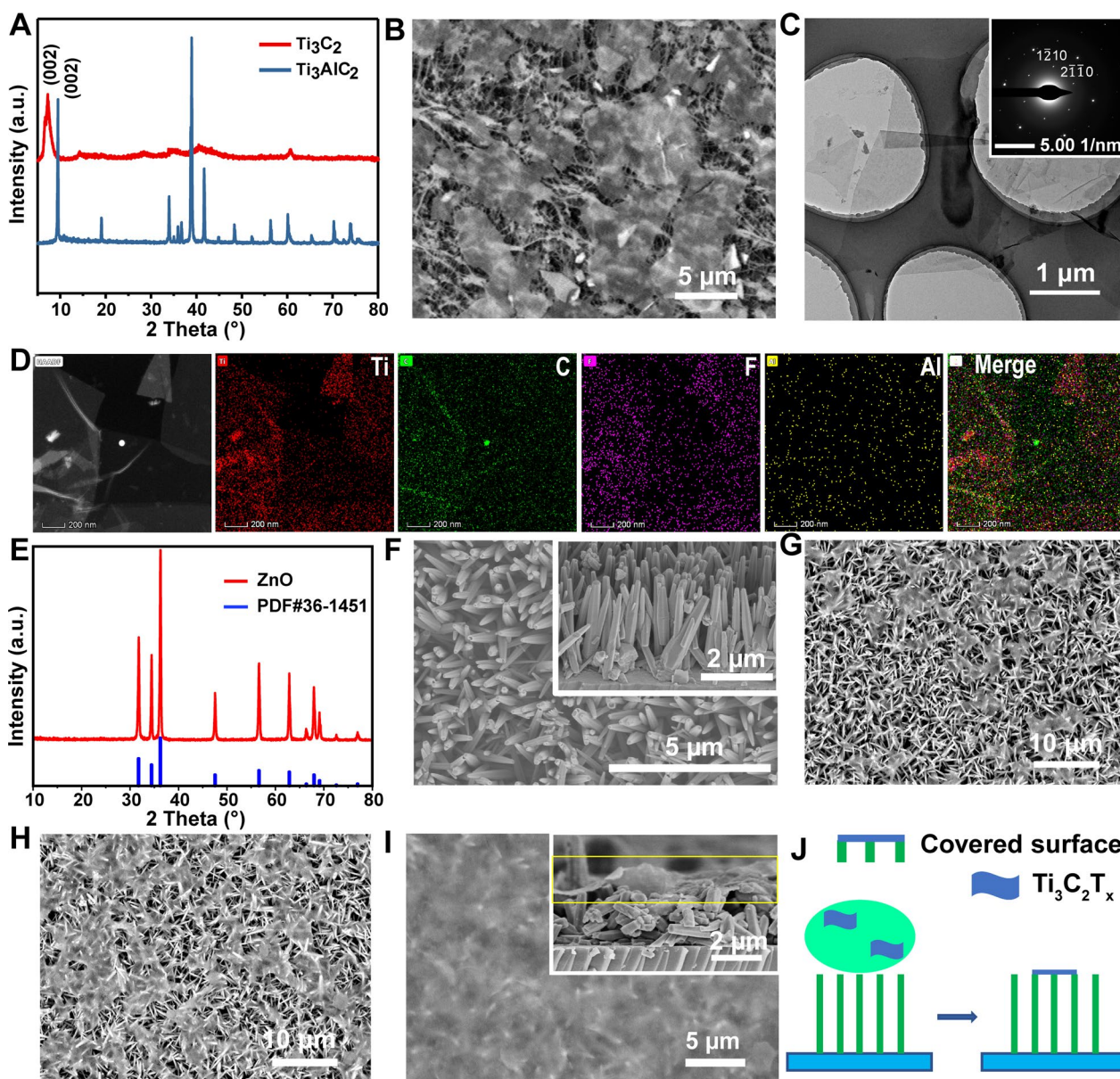
Fig. 2 A X-ray diffraction (XRD) patterns of pristine Ti_3AlC_2 and $Ti_3C_2T_x$. **B** Scanning electron microscopy (SEM) image of a $Ti_3C_2T_x$ monolayer under low magnification. **C** High-resolution transmission electron microscopy image of a $Ti_3C_2T_x$ nanosheet and the corresponding selected area electron diffraction pattern. **D** Scanning TEM (STEM) coupled with energy dispersive X-ray spectroscopy (EDX) of a $Ti_3C_2T_x$ nanosheet. **E** XRD patterns of ZnO nanorod arrays with hexagonal wurtzite structure (Joint Committee on Powder Diffraction Standards card no. 36–1451). **F** SEM image of the ZnO nanorod array without $Ti_3C_2T_x$, and SEM images after drop-casting 4 µL of **G** 1 mg/mL, **H** 1.5 mg/mL, and **I** 2 mg/mL $Ti_3C_2T_x$ solutions on the ZnO nanorod array, the inset is a sectional view of ZnO/$Ti_3C_2T_x$. **J** Illustration of the ZnO/$Ti_3C_2T_x$ substrate fabrication process

(001) and ZnO (101) surfaces were obtained from their corresponding bulk supercell structures. To describe the charge transfer at the interface of these structures, lattice parameters of $a = 12.384727$ and $b = 19.073$ were established. Finally, the molecular adsorption energy (E_b) was calculated using the expression [43] $E_b = E_{total} - E_1 - E_2$, where E_1, E_2, and E_{total} are the respective energies of the interface, molecule, and interface with molecules adsorbed.

Results and discussion
Characterization of $Ti_3C_2T_x$ nanosheets
Two-dimensional $Ti_3C_2T_x$ nanosheets were prepared by selectively etching the Al layer from Ti_3AlC_2. As shown

Wu *et al. Journal of Nanobiotechnology*   (2023) 21:17

Page 5 of 11
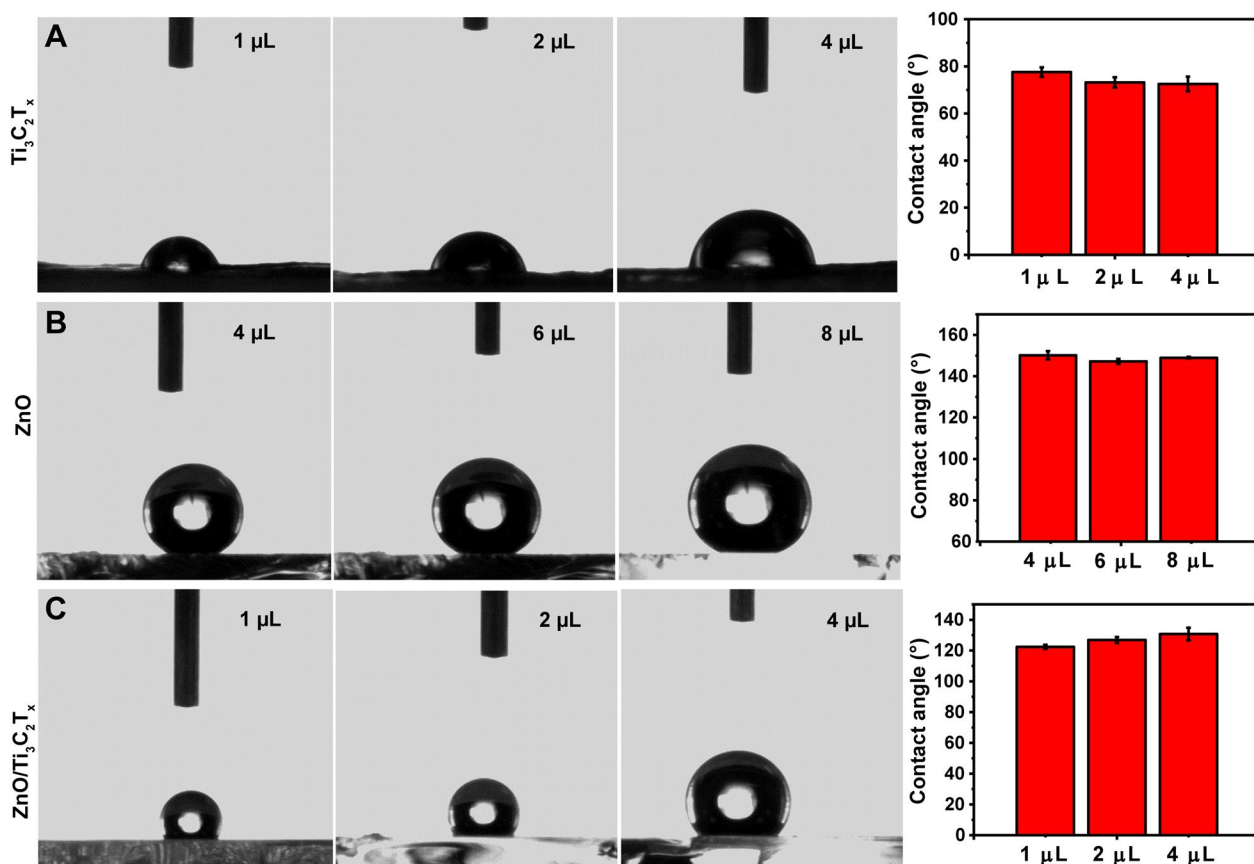
Fig. 3 Characterization of water droplet contact angles on **A** pristine $Ti_3C_2T_x$ film, **B** the ZnO nanorod array, and **C** $ZnO/Ti_3C_2T_x$

by the X-ray powder diffraction (XRD) patterns (Fig. 2A), the main peaks corresponding to MAX-phase Ti_3AlC_2 disappeared after etching, and the (002) diffraction angle decreased from 9.5° to 7.5°. Large $Ti_3C_2T_x$ nanosheets were obtained using an in situ HCl/LiF etching method (Fig. 2B). High-resolution transmission electron microscopy and selected area electron diffraction showed that monolayered $Ti_3C_2T_x$ sheets were successfully derived from MAX-phase Ti_3AlC_2 (Fig. 2C). Elemental composition maps obtained using X-ray energy-dispersive spectroscopy further proved that the Al layer was completely removed from the $Ti_3C_2T_x$ surface (Fig. 2D, Additional file 1: Figure S1). These results demonstrate the successful etching of the atomic Al layer in Ti_3AlC_2.

## Characterization of the $ZnO/Ti_3C_2T_x$ SERS substrate

The ZnO nanorod arrays were prepared using a microfluidic chemical reaction. As shown in Fig. 2E, the XRD spectrum of the prepared ZnO was the same as that of ZnO with hexagonal wurtzite structure. Field emission SEM showed that the inclined ZnO nanorods with a length of ≈2.5 μm and a uniform hexagonal structure

were successfully decorated on the glass substrate (Fig. 2F).

Small-area $ZnO/Ti_3C_2T_x$ spots were prepared by depositing $Ti_3C_2T_x$ solutions on a ZnO nanorod-modified glass substrate. To prevent oxidation of the $Ti_3C_2T_x$, the spots were dried at room temperature. As shown in Fig. 2G–I, the coverage area of the 2D $Ti_3C_2T_x$ nanosheets was improved by increasing the concentration of the $Ti_3C_2T_x$ solution. Furthermore, Fig. 2H shows that the $Ti_3C_2T_x$ nanosheets were supported by the tips of ZnO nanorods and closely attached to the inclined nanorods. With the increasing concentration of $Ti_3C_2T_x$, a thin film gradually formed on the ZnO nanorod array (inset of Fig. 2I). Therefore, $ZnO/Ti_3C_2T_x$ was fabricated by concentrating $Ti_3C_2T_x$ nanosheets on ZnO nanorod arrays surface (Fig. 2J).

Hydrophilicity of prepared substrates

The hydrophilicities of the $Ti_3C_2T_x$ film, ZnO nanorod array, and $ZnO/Ti_3C_2T_x$ were assessed by measuring the surface contact angles of water droplets. The $Ti_3C_2T_x$ film was hydrophilic, having contact angles of $77.6 \pm 2°$ and $72.5 \pm 3°$ for droplet volumes of 1 and 4 μL, respectively
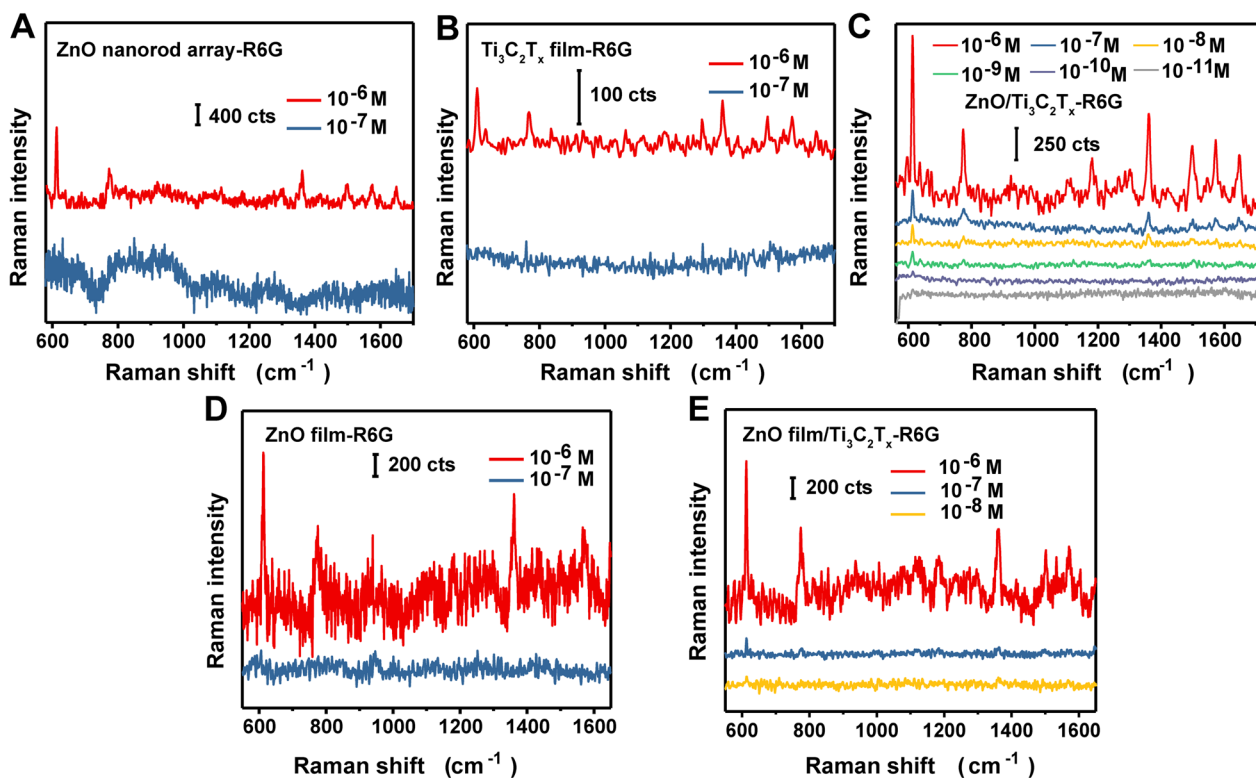
Fig. 4 SERS performance of **A** the superhydrophobic ZnO nanorod array, **B** $Ti_3C_2T_x$ film, **C** ZnO/$Ti_3C_2T_x$ (R6G analyte concentration ranging from 10^{-6} to 10^{-11} M), and **D** ZnO film, **E** ZnO(film)/$Ti_3C_2T_x$ (R6G analyte concentration ranging from 10^{-6} to 10^{-8} M)

(Fig. 3A). The ZnO nanorod array surface was superhydrophobic (Fig. 3B), having a low affinity for droplet volumes less than 4 µL. Even 4 µL droplets maintained a contact angle of $150.2 \pm 2°$ and a relatively spherical shape. Under gravity, droplet volumes of 6 and 8 µL made greater contact with the substrate surface and had an ellipsoidal shape. These results proved that the superhydrophobic substrate was successfully fabricated by decorating the glass slide with the ZnO nanorod array. Coating the ZnO with $Ti_3C_2T_x$ resulted in a contact angle of $130.7 \pm 4°$ for 4 µL droplets (Fig. 3C). Smaller contact angles were observed for droplet sizes less than 4 µL, which may be explained by the micro/nanostructure of ZnO/$Ti_3C_2T_x$. For example, if the droplet is larger than the hydrophilic modification area, the edge of ZnO/$Ti_3C_2T_x$ substrate can still be superhydrophobic. Importantly, ZnO/$Ti_3C_2T_x$ showed a higher hydrophilicity than the ZnO nanorod array, as evidenced by the smaller contact angles and easier droplet attachment. These results demonstrate that the ZnO/$Ti_3C_2T_x$ substrate greatly improved the water droplet attachment and maintained high contact angles after $Ti_3C_2T_x$ modification.

SERS performance of the ZnO/$Ti_3C_2T_x$ substrate

Amorphous ZnO nanocages have remarkable SERS activity [44]. Here, crystalline ZnO also showed SERS activity, with a hexagonal wurtzite ZnO nanorod array yielding an R6G detection limit of 10^{-6} M. As indicated in Fig. 4A, characteristic peaks of R6G can be clearly identified. However, the characteristic Raman scattering peaks at 614, 773, 1360, 1500, 1573, and 1650 cm^{-1} were almost undetectable at an R6G concentration of 10^{-7} M.

An R6G detection limit of 10^{-7} M was achieved using $Ti_3C_2T_x$ film (Fig. 4B), which is consistent with a previously reported value [32]. Different $Ti_3C_2T_x$ films were prepared by filtering $Ti_3C_2T_x$ nanosheets (0.5–2.0 mg in 30 mL water) on a polytetrafluoroethylene membrane (50 mm of diameter). At an R6G concentration of 10^{-6} M, all films had slight difference of SERS activity (Additional file 1: Figure S2). However, reducing the R6G concentration from 10^{-6} to 10^{-7} M resulted in markedly lower intensities of the Raman peaks at 773 and 1500 cm^{-1} and rendered the characteristic peaks at 614, 1360, 1573, and 1650 cm^{-1} undetectable. The SERS activity of the ZnO/$Ti_3C_2T_x$ substrate was much higher than that of pristine ZnO and $Ti_3C_2T_x$, resulting in an R6G detection limit of 10^{-11} M (Fig. 4C) with enhancement factors (EFs) of 1.49×10^7 and 7.88×10^6 at peaks of 614

Wu *et al. Journal of Nanobiotechnology*   (2023) 21:17

Page 7 of 11

and 1360 cm^{-1}, respectively (Additional file 1: Table S1, calculation details were presented in supporting information). The EF of ZnO/Ti$_3$C$_2$T$_x$ is 2.10fold of Ti$_3$C$_2$T$_x$ and 2.73fold of ZnO at peak of 614 cm^{-1}. At 1360 cm^{-1}, the EF of ZnO/Ti$_3$C$_2$T$_x$ is 1.65fold and 2.64fold of Ti$_3$C$_2$T$_x$ and ZnO, respectively. As can be seen in Additional file 1: Figure S6, with the decrease of analyte concentration, the distribution of Raman signal becomes uneven. This indicates that the distribution of molecules on the substrate is not uniform with decreasing concentration. According to the Raman mapping, 10^{-11} M R6G could be detected by mapping method. Thus, the combination of ZnO and Ti$_3$C$_2$T$_x$ enhanced the R6G detection sensitivity by five orders of magnitude compared with that of pristine ZnO and four orders of magnitude compared with that of pristine Ti$_3$C$_2$T$_x$. The ZnO/Ti$_3$C$_2$T$_x$ substrate was also highly sensitive to methylene blue (MB), yielding a detection limit of 10^{-10} M (Additional file 1: Figure S7a).

The SERS performance of the ZnO substrate may be influenced by the ZnO/Ti$_3$C$_2$T$_x$ interfacial properties. A ZnO film and a ZnO(film)/Ti$_3$C$_2$T$_x$ substrate were fabricated to assess the contribution of hydrophobic micro/nanostructure to the SERS activity (Additional file 1: Figure S3a and b). The ZnO film substrate had a higher SERS sensitivity compared with that of pristine ZnO, enabling detection of 10^{-6} M R6G (Fig. 4D). The ZnO(film)/Ti$_3$C$_2$T$_x$ substrate had an even higher SERS sensitivity, achieving an R6G detection limit of 10^{-8} M (Fig. 4E). Contact angle measurements indicated both ZnO film and ZnO(film)/Ti$_3$C$_2$T$_x$ were hydrophilic, displaying 4 μL droplet contact angles of 37.1 ± 1.2° and 77.5 ± 1°, respectively (Additional file 1: Figure S4a and b). The above results demonstrate that the hydrophobic micro/nanostructure of ZnO/Ti$_3$C$_2$T$_x$ may contribute more to the Raman scattering intensity than the hydrophilic micro/nanostructure of ZnO (film)/Ti$_3$C$_2$T$_x$.

DFT calculation of charge transfer properties

To further explore the enhancement mechanism, first-principles DFT calculations were employed. Using the optimized ZnO/Ti$_3$C$_2$T$_x$ (Fig. 5A) and ZnO/Ti$_3$C$_2$T$_x$-R6G (Additional file 1: Figure S5a) interface structures, the charge density difference was calculated. The results clearly identified a charge transfer mechanism at the interface, enabling electron transfer from the ZnO nanorod surface to Ti$_3$C$_2$T$_x$ nanosheet (Fig. 5B). The work of adhesion (W$_{ad}$) describes the relationship between the interface distance and system energy in the interface. The DFT calculations showed that W$_{ad}$ is lowest at an interface distance of ≈2.0 Å (Fig. 5C). This suggests that the distance between ZnO and Ti$_3$C$_2$T$_x$ surfaces is ≈2.0 Å, which results in their chemisorption. The

calculated energy of R6G absorption on the ZnO/Ti$_3$C$_2$T$_x$ interface is −2.36 eV, indicating that the interface has a large adsorption capacity for R6G molecules.

DFT simulations were also carried out to investigate charge transfer phenomena at the interface between Ti$_3$C$_2$T$_x$ and R6G and found that charge can be further transferred from Ti$_3$C$_2$T$_x$ to R6G molecules (Fig. 5D, top view Additional file 1: Figure S5b). These results are consistent with UV–vis spectra of Ti$_3$C$_2$T$_x$-R6G (Fig. 5E), which show difference in the peak position between 500 and 550 nm that could be explained by the chemisorption of Ti$_3$C$_2$T$_x$ and R6G. Moreover, the calculated density of states of ZnO/Ti$_3$C$_2$T$_x$-R6G increased toward the Femi level after adsorption of R6G (Fig. 5F), which again indicates there is interfacial charge transfer between the substrate and R6G. Chemisorption was likewise observed between Ti$_3$C$_2$T$_x$ with MB, together with an obvious absorption peak shift (Fig. 5g), suggesting charge transfer also occurs between Ti$_3$C$_2$T$_x$ and MB and leads to high SERS activity (detection limit of 10^{-10} M). However, because of the physisorption of the AB and CV molecules with the Ti$_3$C$_2$T$_x$ surface, no obvious absorption peak shift was observed (Fig. 5H, I), which could explain why the SERS enhancement of AB and CV is limited (Additional file 1: Figure S7b, c). Considering that the group of ZnO(film)/Ti$_3$C$_2$T$_x$ with a larger contact area between Ti$_3$C$_2$T$_x$ and ZnO film did not show more significant enhancement performance, this suggests that the hydrophobic structure plays a more important role in Raman enhancement. These results suggest that the observed SERS performance of the ZnO/Ti$_3$C$_2$T$_x$ substrate may result from a synergy between its analyte-concentrating ability and interfacial charge transfer properties.

To evaluate the spatial distribution of the SERS intensity, the Raman intensity from 10^{-6} M R6G dropcast on the ZnO/Ti$_3$C$_2$T$_x$ substrate was mapped at 1360 cm^{-1}. The signal distribution on the substrate did not exhibit a coffee ring effect, and its signal was slightly stronger in the depressions than in the protrusions (Fig. 6A and B). To investigate the reason for this phenomenon, we took SEM images of the distribution of gold nanoparticles on the substrate to simulate the distribution of R6G (Fig. 6C). According to the image, gold nanoparticles tend to aggregate more in the depression than elsewhere, so the intensity of the Raman signal in the depression is also slightly stronger than elsewhere. Despite the slightly different molecular distributions, the overall signal intensity remained relatively uniform. Statistical analysis of 1360 cm^{-1} peak intensity in Fig. 6D yielded a relative standard deviation of only 6.23%, which indicates the platform is highly homogeneous and thus capable of providing reproducible signals. Area mapping of 10^{-6} M to 10^{-11} M was

Wu *et al. Journal of Nanobiotechnology*   (2023) 21:17

Page 8 of 11
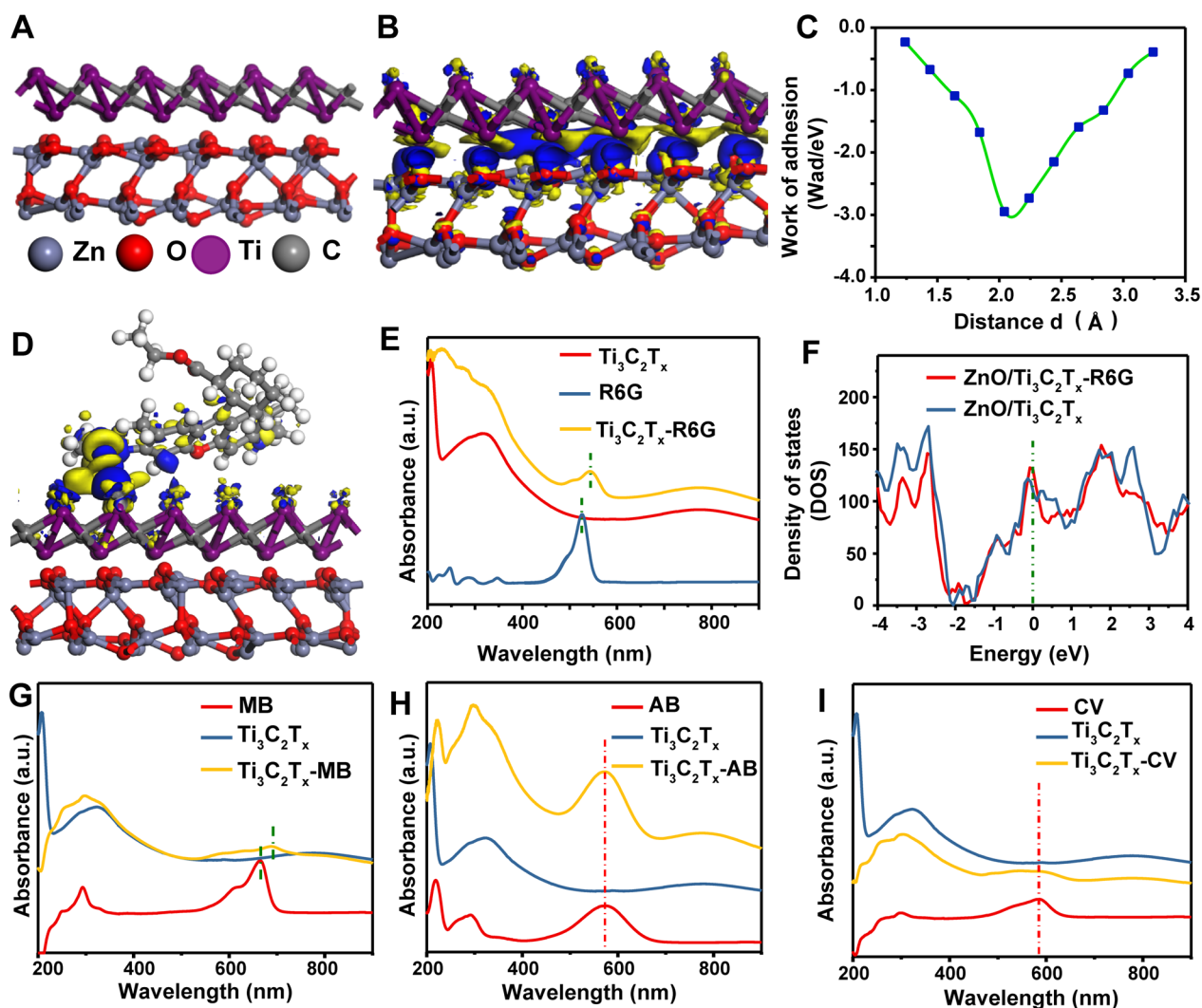
Fig. 5 Density functional theory calculations of molecular properties. **A** Optimized interface structure of ZnO/Ti$_3$C$_2$T$_x$. **B** Calculated charge density difference of ZnO/Ti$_3$C$_2$T$_x$. **C** Work of adhesion at the ZnO/Ti$_3$C$_2$T$_x$ interface. **D** Calculated charge density difference of ZnO/Ti$_3$C$_2$T$_x$-R6G. **E** UV–vis spectra of R6G, Ti$_3$C$_2$T$_x$, and Ti$_3$C$_2$T$_x$-R6G measured by Ultraviolet–visible Spectrophotometer. **F** Density of states of ZnO/Ti$_3$C$_2$T$_x$ and ZnO/Ti$_3$C$_2$T$_x$-R6G. **G–I** UV–vis spectra of (**G**) MB, Ti$_3$C$_2$T$_x$, and Ti$_3$C$_2$T$_x$-MB, (**H**) AB, Ti$_3$C$_2$T$_x$, and Ti$_3$C$_2$T$_x$-AB, and (**I**) CV, Ti$_3$C$_2$T$_x$, and Ti$_3$C$_2$T$_x$-CV measured by Ultraviolet–visible Spectrophotometer

performed as can be seen in Additional file 1: Figure S6, with the decrease of analyte concentration, the distribution of Raman signal becomes uneven. This indicates that the distribution of molecules on the substrate is not that uniform with decreasing concentration, which result in the signal variation. A more reasonable sampling method is to first find the location of the analyte by point measurement, and then do the area mapping based on this, then analyze the area where the signal is more concentrated.

Finally, the ability of the ZnO/Ti$_3$C$_2$T$_x$ substrate to detect biological macromolecules was assessed. Using microRNA as an analyte (Fig. 6e), a detection limit

of 10^{-6} M was obtained and characteristic peaks at 925 cm^{-1} and 1040 cm^{-1} [45] were clearly observed at microRNA concentrations from 10^{-4} to 10^{-6} M. The measured Raman intensities show a certain linear relationship at the two characteristic peaks of 925 cm^{-1} and 1040 cm^{-1} (R$^2_{925\,cm}{}^{-1}=0.9858$, R$^2_{1040\,cm}{}^{-1}=0.9865$) with a detection limit of 10^{-6} M. We speculate that there are two possible causes of this phenomenon. As can be seen in Additional file 1: Figure S7, the distribution of analytes was uneven at low concentration, which result in the uneven distribution of Raman signal. Another possibility is that different nucleobase pairs (U and A) adsorb differently to the substrate [46–48],
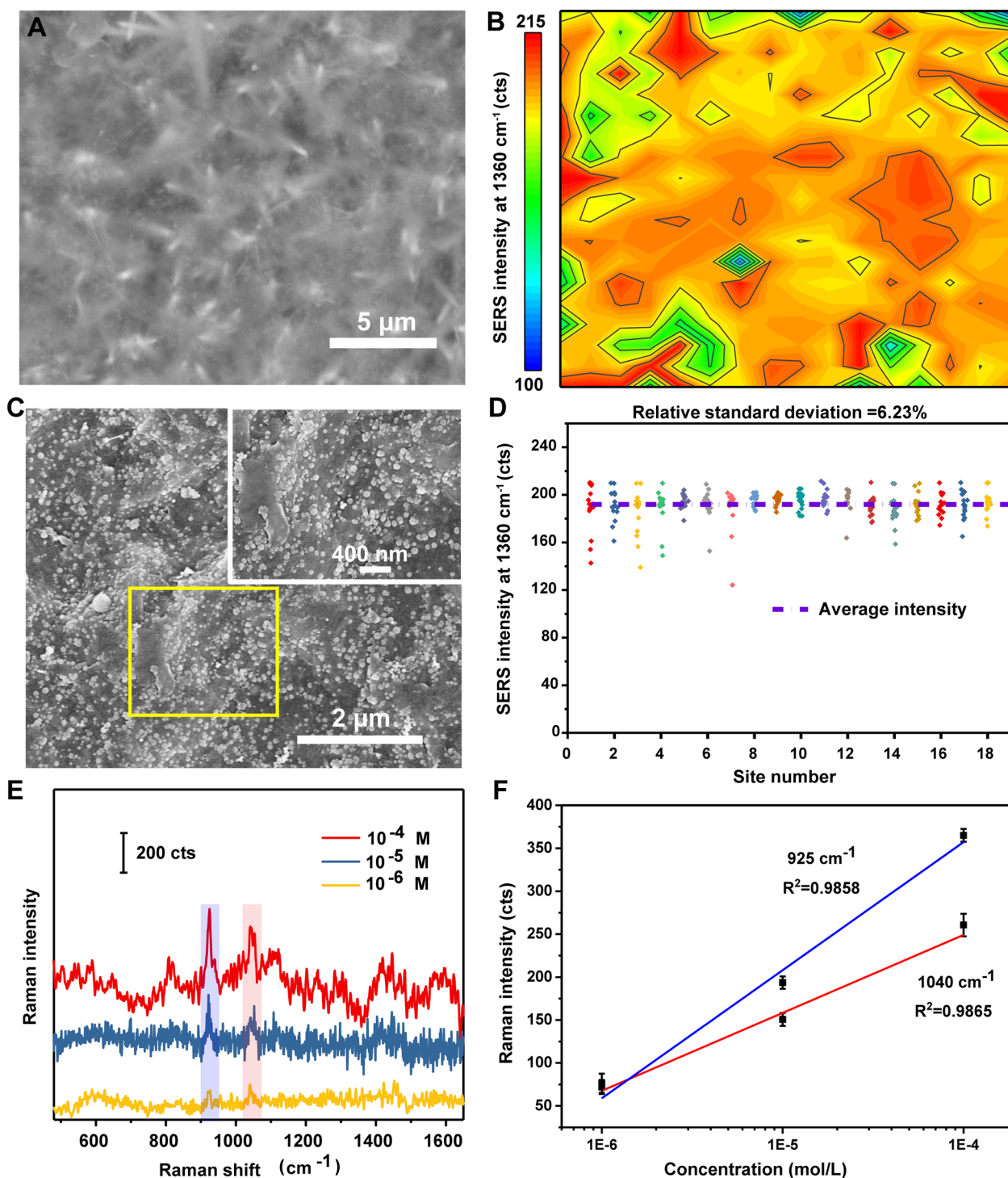
Fig. 6 **A** SEM image of the ZnO/Ti$_3$C$_2$T$_x$ substrate. **B** Spatial map of the SERS intensity (at 1360 cm^{-1}) of 10^{-6} M R6G drop-cast on ZnO/Ti$_3$C$_2$T$_x$ (n = 16 × 18). **C** SEM images of Au nanoparticles distributed on the ZnO/Ti$_3$C$_2$T$_x$ substrate, inset provides the enlarged image of selected section. **D** The SERS intensity distribution of the 1360 cm^{-1} peak across all mapping sites in panel b. **E** SERS spectra of 10^{-4} to 10^{-6} M microRNA on ZnO/Ti$_3$C$_2$T$_x$. **F** Linear fit plots of peaks of 925 cm^{-1} and 1040 cm.$^{-1}$, respectively (n = 9)

Wu *et al. Journal of Nanobiotechnology* (2023) 21:17

Page 10 of 11

resulting in different signal intensities that enhanced by ZnO/Ti$_3$C$_2$T$_x$ substrate. Besides, the ZnO/Ti$_3$C$_2$T$_x$ substrate yielded a much lower Raman intensity than that obtained using a SERS substrate composed of Au nanoparticles (Additional file 1: Figure S8a and b). However, the signal stability of the SERS performance of ZnO/Ti$_3$C$_2$T$_x$ was higher, especially at the peaks of 925 cm^{-1} and 1040 cm^{-1}, characteristic peaks can be clearly identified even at 10^{-6} M, which may result from its greater analyte-concentrating ability compared with that of the hydrophilic Au nanoparticles. The stable SERS performance of ZnO/Ti$_3$C$_2$T$_x$ suggests it may provide a new substrate for biological analyte detection.

Conclusion

In summary, a hydrophobic micro/nanostructured ZnO/Ti$_3$C$_2$T$_x$ SERS substrate was developed and yielded a detection limit of 10^{-11} M using R6G as target analytes. DFT calculations were used to study the mechanism underlying the SERS activity. Synergy between the hydrophobic nanostructure and ZnO/Ti$_3$C$_2$T$_x$ interfacial charge transfer were found to enhance the SERS activity. Moreover, the platform shows potential for miRNA detection. This work provides a new strategy of combining a semiconductor nanoarray with 2D Ti$_3$C$_2$T$_x$ for designing and fabricating high-performance SERS platforms.

Supplementary Information

The online version contains supplementary material available at https://doi.org/10.1186/s12951-022-01756-4.

Additional file 1. Supplementary Material.

Author contributions

YS, YL and YD worked together in designing the conceptualization of this project. YD participated in the guidance of the work throughout the whole process. ZW performed the experiments, drew schematics and wrote the manuscript. DZ assisted in evaluating the results, discussion and editing the manuscript. XH and JL provided the software and calculation. All authors read and approved the final manuscript.

Availability of data and materials

Data availability—the data generated during the current study are available within the article. Supplementary material related to this article can be found in the online version.

Declarations

Competing interests

The authors declare that they have no known competing financial interests or personal relationships that could have appeared to influence the work reported in this paper.

Author details

^{1}State Key Laboratory of Oncogenes and Related Genes, Shanghai Cancer Institute, Renji Hospital School of Medicine, Shanghai Jiao Tong University, Shanghai 200032, China. ^{2}State Key Laboratory for Modification of Chemical Fibers and Polymer Materials, International Joint Laboratory for Advanced Fiber and Low-Dimension Materials, College of Materials Science and Engineering, Donghua University, Shanghai 201620, China. ^{3}State Key Laboratory of Chemical Engineering, School of Chemical Engineering, East China University of Science and Technology, Shanghai 200237, China.

References

1. Liang J, Teng P, Xiao W, He G, Song Q, Zhang Y, et al. Application of the amplification-free SERS-based CRISPR/Cas12a platform in the identification of SARS-CoV-2 from clinical samples. J Nanobiotechnol. 2021;19:273.
2. Bock S, Choi YS, Kim M, Yun Y, Pham XH, Kim J, et al. Highly sensitive near-infrared SERS nanoprobes for in vivo imaging using gold-assembled silica nanoparticles with controllable nanogaps. J Nanobiotechnol. 2022;20:130.
3. Cardinal MF, Vander Ende E, Hackler RA, McAnally MO, Stair PC, Schatz GC, et al. Expanding applications of SERS through versatile nanomaterials engineering. Chem Soc Rev. 2017;46:3886–903.
4. Ding S-Y, You E-M, Tian Z-Q, Moskovits M. Electromagnetic theories of surface-enhanced Raman spectroscopy. Chem Soc Rev. 2017;46:4042–76.
5. Zong C, Xu M, Xu L-J, Wei T, Ma X, Zheng X-S, et al. Surface-enhanced Raman spectroscopy for bioanalysis: reliability and challenges. Chem Rev. 2018;118:4946–80.
6. Langer J, Jimenez de Aberasturi D, Aizpurua J, Alvarez-Puebla RA, Auguié B, Baumberg JJ, et al. Present and future of surface-enhanced Raman scattering. ACS Nano. 2020;14:28–117.
7. Haldavnekar R, Venkatakrishnan K, Tan B. Next generation SERS- atomic scale platform for molecular level detection. Appl Mater Today. 2020;18:100529.
8. Ran P, Jiang L, Li X, Li B, Zuo P, Lu Y. Femtosecond photon-mediated plasma enhances photosynthesis of plasmonic nanostructures and their SERS applications. Small. 2019;15:1804899.
9. Chen R, Du X, Cui Y, Zhang X, Ge Q, Dong J, et al. Vertical flow assay for inflammatory biomarkers based on nanofluidic channel array and SERS nanotags. Small. 2020;16:2002801.
10. Huang JA, Mousavi MZ, Zhao Y, Hubarevich A, Omeis F, Giovannini G, et al. SERS discrimination of single DNA bases in single oligonucleotides by electro-plasmonic trapping. Nat Commun. 2019;10:5321.
11. Lee J, Crampton KT, Tallarida N, Apkarian VA. Visualizing vibrational normal modes of a single molecule with atomically confined light. Nature. 2019;568:78–82.
12. Le Ru EC, Etchegoin PG. Single-molecule surface-enhanced Raman spectroscopy. Annu Rev Phys Chem. 2012;63:65–87.
13. Michaels AM, Nirmal M, Brus LE. Surface enhanced Raman spectroscopy of individual rhodamine 6G molecules on large Ag nanocrystals. J Am Chem Soc. 1999;121:9932–9.
14. Stöckle RM, Suh YD, Deckert V, Zenobi R. Nanoscale chemical analysis by tip-enhanced Raman spectroscopy. Chem Phys Lett. 2000;318:131–6.
15. De Angelis F, Patrini M, Das G, Maksymov I, Galli M, Businaro L, et al. A hybrid plasmonic-photonic nanodevice for label-free detection of a few molecules. Nano Lett. 2008;8:2321–7.
16. Schuller JA, Barnard ES, Cai W, Jun YC, White JS, Brongersma ML. Plasmonics for extreme light concentration and manipulation. Nat Mater. 2010;9:193–204.

Wu *et al. Journal of Nanobiotechnology*   (2023) 21:17

Page 11 of 11

17. De Angelis F, Gentile F, Mecarini F, Das G, Moretti M, Candeloro P, et al. Breaking the diffusion limit with super-hydrophobic delivery of molecules to plasmonic nanofocusing SERS structures. Nat Photonics. 2011;5:682–7.
18. Nair PR, Alam MA. Performance limits of nanobiosensors. Appl Phys Lett. 2006;88:233120.
19. Sheehan PE, Whitman LJ. Detection limits for nanoscale biosensors. Nano Lett. 2005;5:803–7.
20. Eftekhari F, Escobedo C, Ferreira J, Duan X, Girotto EM, Brolo AG, et al. Nanoholes as nanochannels: Flow-through plasmonic sensing. Anal Chem. 2009;81:4308–11.
21. Lassiter JB, Aizpurua J, Hernandez LI, Brandl DW, Romero I, Lal S, et al. Close encounters between two nanoshells. Nano Lett. 2008;8:1212–8.
22. Xiao L, Wang C, Dai C, Littlepage LE, Li J, Schultz ZD. Untargeted tumor metabolomics with liquid chromatography–surface-enhanced Raman spectroscopy. Angew Chemie Int Ed. 2020;59:3439–43.
23. Xu F, Zhang Y, Sun Y, Shi Y, Wen Z, Li Z. Silver nanoparticles coated zinc oxide nanorods array as superhydrophobic substrate for the amplified SERS effect. J Phys Chem C. 2011;115:9977–83.
24. Lee HK, Lee YH, Zhang Q, Phang IY, Tan JMR, Cui Y, et al. Superhydrophobic surface-enhanced Raman scattering platform fabricated by assembly of Ag nanocubes for trace molecular sensing. ACS Appl Mater Interfaces. 2013;5:11409–18.
25. Kao Y-C, Han X, Lee YH, Lee HK, Phan-Quang GC, Lay CL, et al. Multiplex surface-enhanced Raman scattering identification and quantification of urine metabolites in patient samples within 30 min. ACS Nano. 2020;14:2542–52.
26. Li X, Lee HK, Phang IY, Lee CK, Ling XY. Superhydrophobic-oleophobic Ag nanowire platform: an analyte-concentrating and quantitative aqueous and organic toxin surface-enhanced Raman scattering sensor. Anal Chem. 2014;86:10437–44.
27. Du X, Liu D, An K, Jiang S, Wei Z, Wang S, et al. Advances in oxide semiconductors for surface enhanced Raman scattering. Appl Mater Today. 2022;29:101563.
28. Wang ZL. Nanostructures of zinc oxide. Mater Today. 2004;7:26–33.
29. Hu W, Liu Y, Chen T, Liu Y, Li CM. Hybrid ZnO nanorod-polymer brush hierarchically nanostructured substrate for sensitive antibody microarrays. Adv Mater. 2015;27:181–5.
30. Cui H, Liu Q, Li R, Wei X, Sun Y, Wang Z, et al. ZnO nanowire-integrated bio-microchips for specific capture and non-destructive release of circulating tumor cells. Nanoscale. 2020;12:1455–63.
31. Ye Y, Yi W, Liu W, Zhou Y, Bai H, Li J, et al. Remarkable surface-enhanced Raman scattering of highly crystalline monolayer Ti_3C_2 nanosheets. Sci China Mater. 2020;63:794–805.
32. Sarycheva A, Makaryan T, Maleski K, Satheeshkumar E, Melikyan A, Minassian H, et al. Two-dimensional titanium carbide (MXene) as surface-enhanced Raman scattering substrate. J Phys Chem C. 2017;121:19983–8.
33. Li G, Bin GW, Qiu T, Cong S, Zhao Z, Ma R, et al. Surface-modified two-dimensional titanium carbide sheets for intrinsic vibrational signal-retained surface-enhanced Raman scattering with ultrahigh uniformity. ACS Appl Mater Interfaces. 2020;12:23523–31.
34. Li J, Kurra N, Seredych M, Meng X, Wang H, Gogotsi Y. Bipolar carbide-carbon high voltage aqueous lithium-ion capacitors. Nano Energy. 2019;56:151–9.
35. Alhabeb M, Maleski K, Anasori B, Lelyukh P, Clark L, Sin S, et al. Guidelines for synthesis and processing of two-dimensional titanium carbide ($Ti_3C_2T_x$ MXene). Chem Mater. 2017;29:7633–44.
36. Wu Z, Zhao D, Hou C, Liu L, Chen J, Huang H, et al. Enhanced immunofluorescence detection of a protein marker using a PAA modified ZnO nanorod array-based microfluidic device. Nanoscale. 2018;10:17663–70.
37. Zhao D, Wu Z, Zhang W, Yu J, Li H, Di W, et al. Substrate-induced growth of micro/nanostructured Zn(OH)F arrays for highly sensitive microfluidic fluorescence assays. ACS Appl Mater Interfaces. 2021;13:28462–71.
38. Zhao D, Wu Z, Yu J, Wang H, Li Y, Duan Y. Highly sensitive microfluidic detection of carcinoembryonic antigen via a synergetic fluorescence enhancement strategy based on the micro/nanostructure optimization of ZnO nanorod arrays and in situ ZIF-8 coating. Chem Eng J. 2020;383:123230.
39. Li H, Wang J, Liu H, Zhang H, Li X. Zinc oxide films prepared by sol–gel method. J Cryst Growth. 2005;275:e943–6.
40. Blöchl PE. Projector augmented-wave method. Phys Rev B. 1994;50:17953–79.
41. Joubert D. From ultrasoft pseudopotentials to the projector augmented-wave method. Phys Rev B Condens Matter Mater Phys. 1999;59:1758–75.
42. Perdew JP, Burke K, Ernzerhof M. Generalized gradient approximation made simple. Phys Rev Lett. 1996;77:3865–8.
43. Yang Z, Liu G. First-principles study on the influence of compressive deformation on the oxygen adsorption energy and electrical properties of phosphorene. Phys B Condens Matter. 2019;563:72–8.
44. Wang X, Shi W, Jin Z, Huang W, Lin J, Ma G, et al. Remarkable SERS activity observed from amorphous ZnO nanocages. Angew Chemie Int Ed. 2017;56:9851–5.
45. Bell SEJ, Sirimuthu NMS. Surface-enhanced Raman spectroscopy (SERS) for sub-micromolar detection of DNA/RNA mononucleotides. J Am Chem Soc. 2006;128:15580–1.
46. El Amri C, Marie-Helene B, Marie-Christine M. Adenine and RNA in mineral samples. Surface-enhanced Raman spectroscopy (SERS) for picomole detections. Spectrochim Acta A Mol Biomol Spectrosc. 2003;59:2645–54.
47. Driskell JD, Primera-pedrozo OM, Dluhy RA, Zhao Y, Tripp RA. Quantitative surface-enhanced Raman spectroscopy based analysis of MicroRNA mixtures. Appl Spectrosc. 2009;63:1107–14.
48. Driskell JD, Seto AG, Jones LP, Jokela S, Dluhy RA, Zhao Y, et al. Rapid microRNA (miRNA) detection and classification via surface-enhanced Raman spectroscopy (SERS). Biosens Bioelectron. 2008;24:917–22.

Publisher's Note